

Numerical simulation and experimental validation of solids flows in a bubbling fluidized bed

Isaac K. Gamwo ^{a,*}, Yee Soong ^a, Robert W. Lyczkowski ^b

^a *United States Department of Energy, Federal Energy Technology Center, P.O. Box 10940, Pittsburgh, PA 15236-0940, USA*

^b *Argonne National Laboratory, Energy Systems Division, 9700 South Cass Avenue, Argonne, IL 60439-4815, USA*

Received 7 November 1997; received in revised form 18 September 1998

Abstract

A transient two-phase simulation reactor model for describing the hydrodynamics in a bubbling-fluidized bed was performed. A summary of the numerical method refined for over a decade is presented. The hydrodynamic model, based on the two-fluid theory, was validated with regards to the solids flow patterns in a fluidized bed operated under isothermal conditions. The predicted trends compared well with the experimental solids velocity field. The simulation appears to mimic experimental results accurately: both the simulation and the experiment show that the solids motion follows a ‘gulf–stream’ pattern with solids rising upward in the middle of the bed and falling downward near the side walls. The weak vortex patterns observed in the lower portion of the bed have also been simulated. Comparison of predicted and experimental axial solids velocities were in generally good agreement. This good agreement was found to be a function of the solids viscosity and not of the nonuniform inlet gas velocity. © 1999 Elsevier Science S.A.

Keywords: Gas–solids flow; Experimental validation solids flows; Numerical simulation; Bubbling Fluidized bed hydrodynamics

1. Introduction

Fluidized-bed combustors (FBCs) have continued to show promise for burning high-sulfur coal with low SO_x and NO_x emissions, but erosion of in-bed tubes is still hampering the commercialization of the FBC technology. Despite its importance, the exact mechanisms of tube erosion are poorly understood. A major contributing factor to this unsatisfactory state of affairs is the general lack of reliable solids impact velocity data at the tube surface. Such information is crucial for the understanding of erosion [1].

This paper summarizes a time-dependent three-dimensional hydrodynamic model refined for over a decade which can be used to predict solids flow patterns, including solids impact velocity at the tube surface in a fluidized bed. The validity of the hydrodynamic model was evaluated by comparing the predicted solids flow pattern with the experimental results obtained for the ensemble-and-time-averaged solids velocity field. Generally, good agreement between the computed and experimental solids flow patterns and axial velocities was obtained.

2. Hydrodynamic model

The principles of conservation of mass, momentum, and energy are used in the hydrodynamic models of fluidization. The general mass conservation equations and the separate phase momentum equations for transient and isothermal fluid–solids, nonreactive, two-phase flow are written as follows in conservation law form for hydrodynamic model B [2–4].

* Corresponding author. Department of Mechanical Engineering, University of Akron, Akron, OH 44325-3903, USA. Tel.: +1-330-972-7256; Fax: +1-330-972-6027; E-mail: gamwo@uakron.edu

2.1. Conservation equations

Continuity equation for phase n (= g, s):

$$\frac{\partial}{\partial t} (\varepsilon_n \rho_n) + \nabla \cdot (\varepsilon_n \rho_n \vec{v}_n) = 0 \quad (1)$$

Volume fraction constraint:

$$\varepsilon_g + \varepsilon_s = 1.0 \quad (2)$$

Gas-phase momentum equation:

$$\frac{\partial}{\partial t} (\varepsilon_g \rho_g \vec{v}_g) + \nabla \cdot (\varepsilon_g \rho_g \vec{v}_g \vec{v}_g) = -\nabla \cdot (p_g \vec{I}) + \varepsilon_g \rho_g \vec{g} + \nabla \cdot \vec{\tau}_g + \beta_{gs} (\vec{v}_s - \vec{v}_g) \quad (3)$$

Solids-phase momentum equation:

$$\frac{\partial}{\partial t} (\varepsilon_s \rho_s \vec{v}_s) + \nabla \cdot (\varepsilon_s \rho_s \vec{v}_s \vec{v}_s) = -\nabla \cdot (p_s \vec{I}) + \varepsilon_s \rho_s \vec{g} - \nabla \cdot (\rho_s \vec{I}) + \nabla \cdot \vec{\tau}_s + \beta_{sg} (\vec{v}_g - \vec{v}_s) \quad (4)$$

Since the problem is isothermal, no energy equation is required.

3. Constitutive relationships

The constitutive relationships that close the hydrodynamic model are given below.

3.1. Gas–solids drag coefficients

The interphase drag coefficient, $\beta_{gs} = \beta_{sg} = \beta$, is obtained from standard correlations. Below a porosity of 0.8, β is obtained from Ergun's equation; at and above 0.8, it is obtained from Wen and Yu's expression involving the drag coefficient for a sphere, C_d , as discussed by Lyczkowski et al. [5] and Gidaspow [3], for example. These expressions may be summarized as follows:

For $\varepsilon_g < 0.8$:

$$\beta = 150 \frac{\varepsilon_s^2 \mu_g}{\varepsilon_g d_p^2} + 1.75 \frac{\rho_g \varepsilon_s |\vec{v}_g - \vec{v}_s|}{d_p} \quad (5a)$$

For $\varepsilon_g \geq 0.8$:

$$\beta = \frac{3}{4} C_d \frac{\varepsilon_g \varepsilon_s \rho_g |\vec{v}_g - \vec{v}_s|}{d_p} \varepsilon_g^{-2.65} \quad (5b)$$

The drag coefficient, C_d , is given by

$$C_d = \frac{24}{\text{Re}_p} \left[1 + 0.15 \text{Re}_p^{0.687} \right] \quad \text{for } \text{Re}_p < 1000$$

$$C_d = 0.44 \quad \text{for } \text{Re}_p \geq 1000 \quad (6)$$

The particle Reynolds number, Re_p , based on particle diameter is given by

$$\text{Re}_p = \frac{\varepsilon_g \rho_g |\vec{v}_g - \vec{v}_s| d_p}{\mu_g} \quad (7)$$

3.2. Gas- and solids-phase viscous stress

Following Gidaspow [3], it is assumed that the gas and solids phases are Newtonian fluids. Therefore the gas and solids phase viscous stresses, $\vec{\tau}_g$ and $\vec{\tau}_s$ are given by the following expressions.

Gas-phase viscous stress:

$$\vec{\tau}_g = \varepsilon_g \mu_g \left[\nabla \vec{v}_g + (\nabla \vec{v}_g)^T \right] - \frac{2}{3} \varepsilon_g \mu_g \nabla \cdot \vec{v}_g \vec{I} \quad (8)$$

Solids-phase viscous stress

$$\bar{\tau}_s = \varepsilon_s \mu_s \left[\nabla \vec{v}_s + (\nabla \vec{v}_s)^T \right] - \frac{2}{3} \varepsilon_s \mu_s \nabla \cdot \vec{v}_s \bar{I} \quad (9)$$

3.3. Solids-phase pressure

In the solids-phase momentum equation, (4), p_s is the solids-phase pressure resulting from particle-to-particle interactions. A general formulation of such a term would include the effects of porosity, pressure, and the displacement tensors of solids velocity, gas velocity and relative velocity. No such formulation with appropriate material constants is available in the literature to our knowledge. This solids-phase pressure is physically necessary to prevent the particles from compacting to unrealistically low gas-phase volume fractions below that of a packed-bed state, typically 0.36–0.4. The static normal component of the solids-phase pressure, usually called the solids elastic modulus, $G(\varepsilon_s)$, has been used by Pritchett et al. [6], Padhye and O'Brien [7], Syamlal and Gidaspow [8], Gidaspow and Ettehadieh [9], Gidaspow et al. [10–12], Gidaspow [3] and Concha and Bustos [13], for example. $G(\varepsilon_s)$ is related to p_s by the following expression:

$$\nabla \cdot (p_s \bar{I}) = G(\varepsilon_s) \bar{I} \cdot \nabla \varepsilon_s \quad (10)$$

The solids elastic modulus, $G(\varepsilon_s)$, is quite small at and above minimum fluidization (in fact, theoretically it should be 0), but it becomes increasingly important as the particles defluidize or are compressed and are constrained to move. In fact, $G(\varepsilon_s)$ acts as a repulsive pressure at such solids-phase volume fractions. Molerus [14] interpreted this phenomenon as the direct result of Hertz's contact pressure, which is a function of the particle Young's elasticity modulus. This interpretation allows us to relate solids stress measurements to material properties of the powder.

The measurement of this term has been reported by Rietema and Mutsers [15] and by Piepers et al. [16]. There is a considerable disagreement as to the exact form of this stress. Shinohara [17] summarizes 15 different expressions correlating the solids repulsive pressure with the bulk solids-phase volume fraction. Unfortunately, most of these relations lack any strong physical basis.

To place the solids elastic modulus in perspective, we must consider the mechanisms of particulate compaction in agglomeration [17,18]. The motivation for the most generally satisfactory expression is the experimental observation that plotting the logarithm of consolidating pressure vs. volume yields a substantially straight line for both metallic and non metallic powders undergoing compaction. Bouillard et al. [2], used this simple theory to derive a generalized solids elastic modulus expression, $G(\varepsilon_s)$, of the form

$$G(\varepsilon_s) = G_0 \exp[c(\varepsilon_s - \varepsilon_g^*)] = G_0 \exp[-c(\varepsilon_g - \varepsilon_g^*)] \quad (11)$$

where c (called the compaction modulus) is the slope of $\ln(G)$ vs. ε_g , and ε_g^* is the compaction gas volume fraction. The normalization units factor, G_0 , has been taken to be 1.0 Pa for convenience. For $\varepsilon_g > \varepsilon_g^*$, the elasticity modulus G becomes larger as ε_g decreases, thus preventing the solids volume fractions from being larger than $1 - \varepsilon_g^* = \varepsilon_s^*$.

In our work, the compaction modulus c and the compaction volume fraction ε_g^* are 600 and 0.376, respectively from Bouillard et al. [2]. We used this relatively high compaction modulus and low compaction porosity because of the greater compaction resulting from solids striking obstacles in the fluidized bed such as immersed tubes.

3.4. Equations of state

The equations of state for the gas and the solids phases are given in the computer program by simple expressions that can be easily changed to reflect more complicated functional relationships. The expressions used, in terms of the computer program's internal cgs units, are as follows:

$$\rho_g = D_1 + D_2 T + \frac{p_g}{D_3 T}, \quad [\text{g/cm}^3] \quad (12)$$

$$\rho_s = E_1 + E_2 T + \frac{p_g E_3}{T}, \quad [\text{g/cm}^3] \quad (13)$$

where T is the temperature (298.16 K in our problem) and p_g the gas pressure in dynes/cm². In our study, we set D_1 , D_2 , E_2 , and E_3 to 0; $D_3 = R/M$, where M is the average molecular weight of the gas-phase of 29 g/(g mol), R is the universal gas constant equal to 8.314×10^7 erg/(g mol K), and $E_1 = 2.49$ g/cm³.

The conservation equations together with the constitutive relations are solved in the Cartesian coordinate system: calculations are two-dimensional in the x - and y -directions. The gravity vector, \vec{g} , may be oriented in any direction in the two-dimensional computing plane prescribing its components g_x and g_y in the computer program input.

The system of conservation equations ((1), (3) and (4)) form six nonlinear, coupled, partial differential equations in two dimensions that must be solved for the six dependent variables: the gas-phase volume fraction, ε_g , the gas pressure, p_g , the gas velocity components u_g and v_g and the solids velocity components u_s and v_s in the x - and y - directions, respectively.

We need appropriate boundary and initial conditions for the dependent variables listed above to solve the system of equations ((1), (3) and (4)). For setting the initial conditions, the reactor is divided into two regions: the bed and the freeboard. For each of the regions specified above, an initial condition is specified. In the bed region, the gas-phase volume fractions, and axial (x) velocities are set to minimum fluidization conditions, 0.41 and 19.5 cm/s, respectively. The transverse (y) gas velocities and all solids velocity components are set to 0. The pressure is initiated to be the weight of the bed added to the exit pressure. In the freeboard region, the gas-phase volume fractions are set to 1.0, axial gas velocities to 47.6 cm/s, all solids velocities components to 0, and the gas pressure, p_g , to the weight of the free board gas column added to the exit pressure.

No assumption of symmetry was made, thus the computations were carried out for the entire bed. The rigid walls are no-slip walls. Inlet conditions are specified for the fluidizing gas inflow boundary plane. These will be discussed in Section 5. As to the outflow boundary, the gradients of all variables in the axial direction are set to 0 except for the pressure which is set to 101.3 kPa. The inlet pressure is set to this value plus 120% of the weight of the entire bed. The gas viscosity used was 1.82×10^{-5} Pa s, the solids viscosity used is discussed in Section 5.

4. Finite difference equations

Numerical solutions to the conservation equations ((1), (3) and (4)) must be obtained, because the complexity of these field equations makes obtaining exact solutions unlikely. To obtain these numerical solutions, finite-difference equations that are consistent approximations to the field equations must be obtained and solved. Such finite-difference equations are presented and discussed in Appendix A.

5. Comparison with experimental data

The model described above was used to predict the solids flow patterns and velocities in a fluidized bed with tube banks. Ai [19] measured the ensemble-and-time-averaged solids velocity field in a similar bed using a unique radioactive particle tracking technique which is summarized in Gamwo [20], Lyczkowski et al. [21], and Gamwo et al. [22] who also present the details of the experiment and its simulation, the highlights of which will only be summarized herein. Before they analyzed the ensemble and time-averaged solids velocity data and power spectra of the static pressure fluctuations, a careful study was performed to assess the numerical convergence and accuracy of the computations.

The conditions of the experimental simulation are given in Table 1. The inlet superficial gas velocity was first maintained at $0.9 U_{mf}$ for 1.0 s, where U_{mf} was taken to be 19.5 cm/s as determined from the Ergun equation programmed in the computer program. This was done to obtain a reasonable initial condition for the subsequent run at $U/U_{mf} = 2.0$. The timestep used in all the runs was 5×10^{-5} s. Very little difference in results could be seen using time-averaging periods of 1–4 s.

The geometric model reported treated the round tubes as squares, with $18 \times 42 = 756$ total cells in one model and $34 \times 82 = 2788$ total cells in the other. These totals include the ‘dummy’ cells around the periphery of the physical

Table 1
Simulation operating conditions for bed with five tubes

Material	Glass beads
Particle mean diameter (μm)	460
Particle density (g/cm^3)	2.49
Particle sphericity	1.0
Minimum fluidization porosity	0.41
Fluid carrier	Air
Temperature (K)	300
Pressure (kPa, top of the bed)	101.3
Minimum fluidization velocity, U_{mf} (cm/s)	19.5
Fluidization velocity U (cm/s)	39.0
U/U_{mf}	2.0

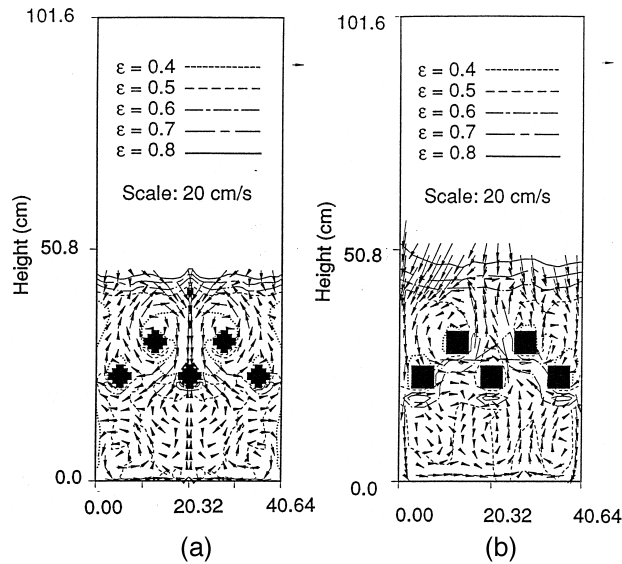


Fig. 1. Computed time-averaged solids velocity vector and porosity contour plots. (a) Symmetry assumption, uniform inlet-gas flow, fine mesh. (b) No symmetry assumption, non uniform inlet-gas flow, coarse mesh.

boundary. The number of computational cells was therefore $16 \times 40 = 640$ and $32 \times 80 = 2560$. A solids viscosity of 0.1 Pa s was used. No assumption of symmetry was made. The reason for this decision was based on preliminary unpublished results shown in Fig. 1a, using an even finer grid treating the tubes as more nearly circular 6×6 obstacles, but assuming symmetry. By comparing Fig. 1a and Fig. 1b, it is clear that the symmetry assumption causes solids to fall down along the line of symmetry above the middle tube, causing even more disagreement with the solids flow patterns than the square tubes. Since it was impractical to continue the convergence study not assuming symmetry with this geometric model because of long computer run times, the numerical convergence and accuracy studies were subsequently performed using the square tube models. This is a reasonable approximation since the main solids flow direction in the experiment is axial as can be seen in Fig. 2b.

All results presented were averaged over 1 s. An essentially grid independent solution was demonstrated using a very tight convergence, 10^{-7} vs. the default value of 5×10^{-4} in the computer program, 3.5 orders of magnitude more accurate Lyczkowski et al. [21]. The convergence parameter controls the pressure-adjustment iteration and depends on how well the gas-phase continuity equation is satisfied. With a tight convergence, much more accurate local mass balances are achieved. The tight convergence results were decidedly more symmetric than the loose convergence results. However, they differed from the data.

Because the standard deviation of the solids velocity data differed significantly from position to position in the bed, it was suspected that there were nonuniformities in the inlet-gas distribution. On the basis of physical arguments, it was decided to increase the inlet-gas flow in the central portion of the bed. This is reasonable because solids tend to come down the sidewalls, obstructing the gas flow there. The gas flow in the central half was increased 30% from the average, and the gas flow near the sidewalls was decreased 30%, so that the total gas flow was the same as in the experiment. As shown in

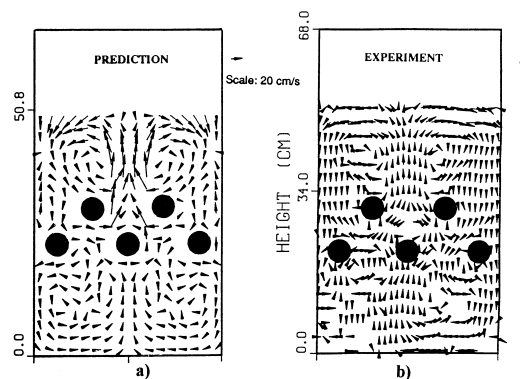


Fig. 2. Comparison of predicted (a) and experimental (b) solids flow pattern.

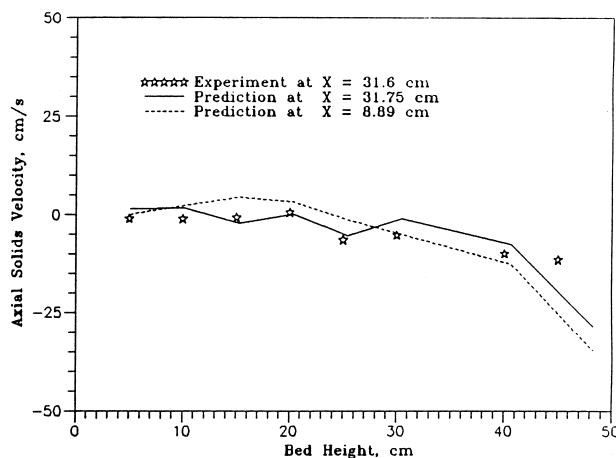


Fig. 3. Computed and experimental solids velocities at $X = 31$ cm.

Fig. 1b, most of the solids flow patterns now agreed qualitatively with the data, but they did not agree quantitatively. Although the possibility for inlet-gas flow nonuniformities may exist, it was therefore ruled out as the major reason for the disagreement with the data.

Rietema [23] conducted an exhaustive literature survey for the effective solids viscosity. In our model, this corresponds to $\varepsilon_s \mu_s$. He concluded that the value is on the order of 0.01 to 1.0 Pa s (0.1 to 10 poise), and that it decreases with increasing gas fluidizing velocity (increasing porosity) and decreases with decreasing mean particle diameter. For the conditions closest to those in the present experiment, a value of 5.9 Pa s (59 poise) is reported by Singh et al. [24]. A value for microscopic solids viscosity of 5 Pa s (50 poise) was chosen. The maximum effective solids viscosity is therefore 0.59×5.0 Pa s = 2.95 Pa s (29.5 poise). Fig. 2a,b shows the comparison between the computed time-averaged solids flow patterns and the measured data for uniform air superficial velocity. Both the experiment and the prediction show that the solids motion follows a ‘gulf–stream’ pattern; with the solids rising upward in the middle of the bed and falling downward near the walls. The vortices observed in the bed beneath the lower tube row have also been predicted. The observed and predicted time-averaged expanded bed heights are in close agreement with each other. Fig. 3 shows a quantitative comparison of the computed axial solids velocity profiles with the experimental values at horizontal distances from the center of $X = 8.89$ and $X = 31.75$ cm. Very good agreement exists between the data and the computations near the bed walls. In the vicinity of the tube, computed solids axial velocities are higher than the data. This could be due to three-dimensional effects or lack of lift forces.

6. Conclusions

The hydrodynamic model of fluidization was adopted to analyze time-averaged solids velocities in a fluidized bed containing a triangular pitch tube array consisting of five round cylinders. The numerical method refined for over a decade was summarized using new compact notation for the first time to the authors’ knowledge. Computed solids flow patterns are physically plausible and generally agree with the experimental data. This generally good agreement was found to be a result of better solids rheology and not nonuniform inlet gas velocity. Both the experiment and the prediction show solids generally ascending near the bed center and descending near the wall. Even the vortices observed in the right lower part of the bed are predicted. Computed axial solids velocity profiles agree with the experimental values. However, complicated patterns near the distributor has not been reproduced adequately. This discrepancy is under investigation and may be due to the three-dimensional effects or lack of lift forces in the model.

7. List of symbols

C_d	Drag coefficient given by Eqs. (5b) and (6)
c	Compaction modulus
d_p	Particle diameter (m)
\vec{g}	Acceleration due to gravity (m/s^2)
G	Solids elastic modulus (Pa)

\bar{I}	Unit tensor
M	Average molecular weight of the gas phase (g/(g mol))
N	Total number of phases
p	Pressure (Pa)
R	Universal gas constant = 8.314×10^7 erg/(g mol K)
Re_p	Particle Reynolds number given by Eq. (7)
T	Temperature (K)
\vec{v}	Velocity vector (m/s)
t	Time (s)
u	x -component of velocity (m/s)
v	y -component of velocity (m/s)
w	z -component of velocity (m/s)
<i>Greek letters</i>	
β	Gas–solids drag coefficient, $= \beta_{gs} = \beta_{sg}$, given by Eqs. (5a) and (5b)
ε	Volume fraction
ε^*	Compaction volume fraction
μ	Shear viscosity (Pa s)
ρ	Density (g/cm ³)
$\bar{\tau}$	Stress
<i>Subscripts</i>	
c	Coulombic
g	Gas phase
n	Phase n (= g, s)
p	Particle
s	Solids phase
i, j, k	Referring to the x, y , and z directions
<i>Superscripts</i>	
T	Transpose
n	Index for time step

Acknowledgements

Thanks to R.R. Anderson, F. Harke, K.R. Mundorf, and G. Jian for their assistance in the preparation of the manuscript.

Appendix A. Numerical method description

The representation of the fields with these finite-difference equations is accomplished by using a completely Eulerian mesh of finite-difference cells. In Cartesian coordinates (x, y), these cells are rectangles with dimensions δ_x and δ_y (Fig. 4).

The essence of the numerical method known as the implicit multifield (IMF) technique was developed by Harlow and Amsdem [25] and was implemented in the KFIX code [26] with minor modifications. Rivard and Torrey [27] later extended

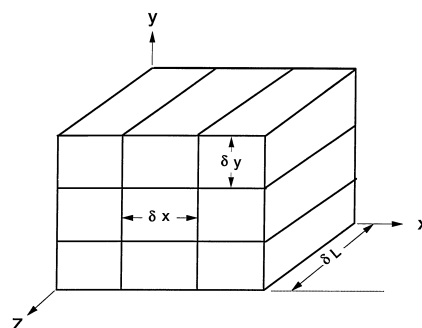


Fig. 4. Cartesian coordinates.

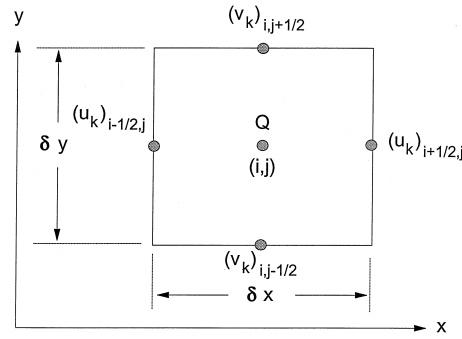


Fig. 5. Typical computational cell, showing the location of quantities occurring in the finite-difference equations.

the IMF numerical method to three dimensions. The method was later adapted and refined for describing gas–solids flows for over a decade by Gidaspow and Ettehadieh [9], Syamlal [28], Syamlal and Gidaspow [8]; Bouillard et al. [2]; Syamlal et al. [29] and Gamwo [20], for example. The refined model validations have been reviewed by Enwald et al. [30] who also reviewed other model validations. They concluded that the model summarized herein is more accurate than others.

A typical two-dimensional x – y plane computational cell, cell (i,j) , in Cartesian coordinates and the relative spatial locations of the quantities that appear in the finite-difference equations are shown in Fig. 5. In this figure and in subsequent figures, the x -components of the gas and solids velocities are denoted by u_k and the y -components are denoted by v_k . The indexes i and j that label cell (i,j) count cell centers in the x and y directions, respectively, and assume only positive integer values. In Fig. 5 and elsewhere, half-integer indexes denote cell edge positions. The scalar variables, collectively denoted by Q in Fig. 5, are stored at the cell centers and the components of velocity vector are stored at the center of cell boundaries. The equations for scalar quantities, pressure, void fraction, and density are solved at the cell centers. The equations for the phase velocity vector components are solved at the cell edges.

The finite-difference approximations to the field equations form a system of nonlinear algebraic equations relating quantities at time $t = (n + 1)\delta t$, where n is 0 or a positive integer and δt is the time increment by which these quantities advance each computational cycle.

The finite-difference approximations to terms that are the divergence of a scalar multiplied by a velocity are obtained by donor-cell differencing. This donor-cell differencing assists in the elimination of numerical instability resulting from

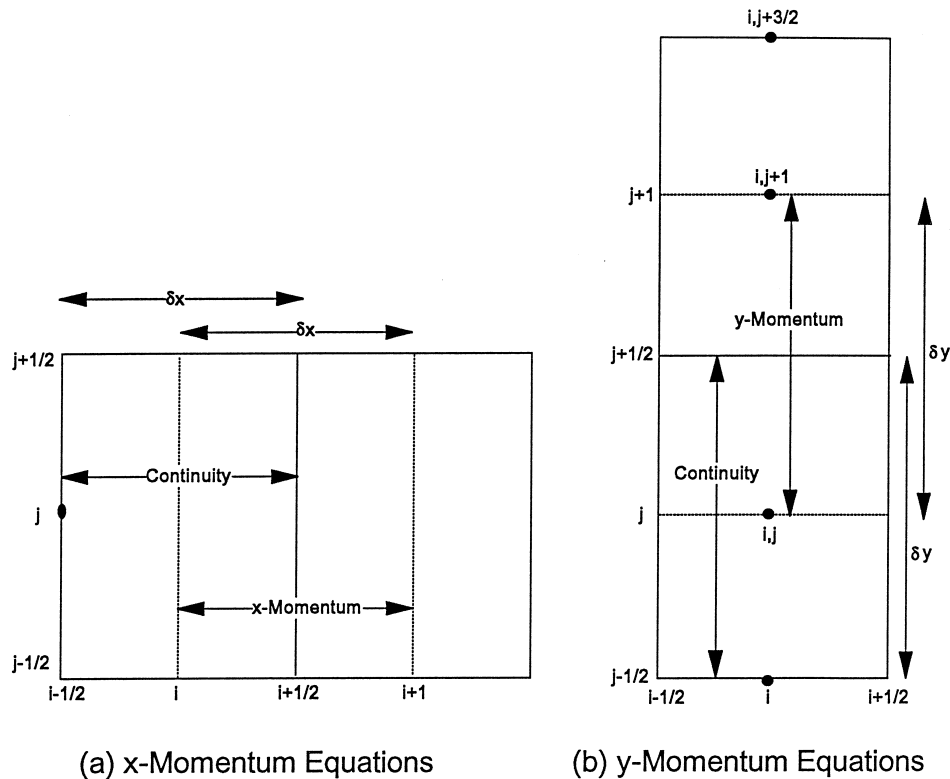


Fig. 6. The staggered computational mesh for momentum equations.

truncation errors without the use of artificial diffusion. The transient two-dimensional computer program used here is a pilot version of the three dimensional IFAP3DB computer program [19]. Since the numerical solutions are essentially the same for the two computer programs, the three-dimensional finite-difference equations and solution technique are included herein, for generality. The subscripts i, j, k correspond to the x, y , and z directions respectively. In addition, the formalism for n phases where $n = 1 = g$ represents the gas phase and $n = 2, 3, \dots, N$ denotes the solids phases is presented for generality.

A.1. The finite difference equations

The computations are carried out using a mesh of finite-difference cells fixed in space (Eulerian Mesh). A typical staggered computational cell at X - Z plane is shown in Fig. 6.

The continuity equation is differenced fully implicitly as follows.

$$(\varepsilon_n \rho_n)_{i,j,k}^{n+1} = (\varepsilon_n \rho_n)_{i,j,k}^n - \frac{\delta t}{\delta x_i} \langle (\varepsilon_n \rho_n) u_n \rangle_{i,j,k}^{n+1} - \frac{\delta t}{\delta y_j} \langle (\varepsilon_n \rho_n) v_n \rangle_{i,j,k}^{n+1} - \frac{\delta t}{\delta z_k} \langle (\varepsilon_n \rho_n) w_n \rangle_{i,j,k}^{n+1} \quad (14)$$

The angular brackets represents a donor cell differencing as shown below.

$$\langle \phi u_n \rangle_{i,j,k} = (u_n)_{i+\frac{1}{2},j,k} \begin{cases} \phi_{i,j,k} & \text{if } (u_n)_{i+\frac{1}{2},j,k} \geq 0; \\ \phi_{i+1,j,k} & \text{if } (u_n)_{i+\frac{1}{2},j,k} < 0. \end{cases} \quad (15a)$$

$$- (u_n)_{i-\frac{1}{2},j,k} \begin{cases} \phi_{i-1,j,k} & \text{if } (u_n)_{i-\frac{1}{2},j,k} \geq 0; \\ \phi_{i,j,k} & \text{if } (u_n)_{i-\frac{1}{2},j,k} < 0. \end{cases}$$

$$\langle \phi v_n \rangle_{i,j,k} = (v_n)_{i,j,k+\frac{1}{2}} \begin{cases} \phi_{i,j,k} & \text{if } (v_n)_{i,j,k+\frac{1}{2}} \geq 0; \\ \phi_{i,j+1,k} & \text{if } (v_n)_{i,j,k+\frac{1}{2}} < 0. \end{cases} \quad (15b)$$

$$- (v_n)_{i,j,k-\frac{1}{2}} \begin{cases} \phi_{i,j-1,k} & \text{if } (v_n)_{i,j,k-\frac{1}{2}} \geq 0; \\ \phi_{i,j,k} & \text{if } (v_n)_{i,j,k-\frac{1}{2}} < 0. \end{cases}$$

and

$$\langle \phi w_n \rangle_{i,j,k} = (w_n)_{i,j,k+\frac{1}{2}} \begin{cases} \phi_{i,j,k} & \text{if } (w_n)_{i,j,k+\frac{1}{2}} \geq 0; \\ \phi_{i,j,k+1} & \text{if } (w_n)_{i,j,k+\frac{1}{2}} < 0. \end{cases} \quad (15c)$$

$$- (w_n)_{i,j,k-\frac{1}{2}} \begin{cases} \phi_{i,j,k-1} & \text{if } (w_n)_{i,j,k-\frac{1}{2}} \geq 0; \\ \phi_{i,j,k} & \text{if } (w_n)_{i,j,k-\frac{1}{2}} < 0. \end{cases}$$

where ϕ is a scalar or a vector quantity.

The momentum equations are differenced over a staggered mesh of computational cells as shown in Fig. 6. The difference equations are given by ($n = g, s$):

$$(\varepsilon_n \rho_n u_n)_{i+\frac{1}{2},j,k}^{n+1} = (\varepsilon_n \rho_n u_n)_{i+\frac{1}{2},j,k}^n - \frac{\delta t}{\delta x_{i+\frac{1}{2}}} ((p_n)_{i+1,j,k} - (p_n)_{i,j,k})^{n+1} + \delta t \sum_{l=1}^N \beta_{i+\frac{1}{2},j,k}^n (u_l - u_n)_{i+\frac{1}{2},j,k}^{n+1} \quad (16a)$$

$$(\varepsilon_n \rho_n v_n)_{i,j,k+\frac{1}{2}}^{n+1} = (\varepsilon_n \rho_n v_n)_{i,j,k+\frac{1}{2}}^n - \frac{\delta t}{\delta y_{j+\frac{1}{2}}} ((p_n)_{i,j+1,k} - (p_n)_{i,j,k})^{n+1} + \delta t \sum_{l=1}^N \beta_{i,j+\frac{1}{2},k}^n (v_l - v_n)_{i,j+\frac{1}{2},k}^{n+1} \quad (16b)$$

$$(\varepsilon_n \rho_n w_n)_{i,j,k+\frac{1}{2}}^{n+1} = (\varepsilon_n \rho_n w_n)_{i,j,k+\frac{1}{2}}^n - \frac{\delta t}{\delta z_{k+\frac{1}{2}}} ((p_n)_{i,j,k+1} - (p_n)_{i,j,k})^{n+1} + \delta t \sum_{l=1}^N \beta_{i,j,k+\frac{1}{2}}^n (w_l - w_n)_{i,j,k+\frac{1}{2}}^{n+1} \quad (16c)$$

All the explicit terms have been lumped into the tilde quantities as shown below.

$$\begin{aligned} (\overline{\varepsilon_n \rho_n u_n})_{i+\frac{1}{2},j,k}^n &= (\varepsilon_n \rho_n u_n)_{i+\frac{1}{2},j,k}^n - \frac{\delta t}{\delta x_{i+\frac{1}{2},j,k}} \langle (\varepsilon_n \rho_n u_n) u_n \rangle_{i+\frac{1}{2},j,k} - \frac{\delta t}{\delta y_j} \langle (\varepsilon_n \rho_n u_n) v_n \rangle_{i+\frac{1}{2},j,k} \\ &\quad - \frac{\delta t}{\delta z_k} \langle (\varepsilon_n \rho_n u_n) w_n \rangle_{i+\frac{1}{2},j,k} + \delta t \varepsilon_n \rho_n g_n + \delta t (\nabla \tau_{nx})_{i+\frac{1}{2},j,k}^n \end{aligned} \quad (17a)$$

$$\begin{aligned} (\overline{\varepsilon_n \rho_n v_n})_{i,j+\frac{1}{2},k}^n &= (\varepsilon_n \rho_n v_n)_{i,j+\frac{1}{2},k}^n - \frac{\delta t}{\delta x_i} \langle (\varepsilon_n \rho_n v_n) u_n \rangle_{i,j+\frac{1}{2},k} - \frac{\delta t}{\delta y_j} \langle (\varepsilon_n \rho_n v_n) v_n \rangle_{i,j+\frac{1}{2},k} \\ &\quad - \frac{\delta t}{\delta z_k} \langle (\varepsilon_n \rho_n v_n) w_n \rangle_{i,j+\frac{1}{2},k} + \delta t \varepsilon_n \rho_n g_y + \delta t (\nabla \tau_{ny})_{i,j+\frac{1}{2},k}^n \end{aligned} \quad (17b)$$

$$\begin{aligned} (\overline{\varepsilon_n \rho_n w_n})_{i,j,k+\frac{1}{2}}^n &= (\varepsilon_n \rho_n w_n)_{i,j,k+\frac{1}{2}}^n - \frac{\delta t}{\delta x_i} \langle (\varepsilon_n \rho_n w_n) u_n \rangle_{i,j,k+\frac{1}{2}} - \frac{\delta t}{\delta y_j} \langle (\varepsilon_n \rho_n w_n) v_n \rangle_{i,j,k+\frac{1}{2}} \\ &\quad - \frac{\delta t}{\delta z_k} \langle (\varepsilon_n \rho_n w_n) w_n \rangle_{i,j,k+\frac{1}{2}} + \delta t \varepsilon_n \rho_n g_z + \delta t (\nabla \tau_{nz})_{i,j,k+\frac{1}{2}}^n \end{aligned} \quad (17c)$$

where

$$\begin{aligned} (\nabla \tau_{nx})_{i+\frac{1}{2},j,k} &= \frac{1}{\delta x_{i+\frac{1}{2},j,k}} [(\tau_{nxx})_{i+1,j,k} - (\tau_{nxx})_{i,j,k}] + \frac{1}{\delta y_j} \left[(\tau_{nxy})_{i+\frac{1}{2},j+\frac{1}{2},k} - (\tau_{nxy})_{i+\frac{1}{2},j-\frac{1}{2},k} \right] \\ &\quad + \frac{1}{\delta z_k} \left[(\tau_{nxz})_{i+\frac{1}{2},j,k+\frac{1}{2}} - (\tau_{nxz})_{i+\frac{1}{2},j,k-\frac{1}{2}} \right] \end{aligned} \quad (18a)$$

$$\begin{aligned} (\nabla \tau_{ny})_{i,j+\frac{1}{2},k} &= \frac{1}{\delta x_i} \left[(\tau_{nxy})_{i+\frac{1}{2},j+\frac{1}{2},k} - (\tau_{nxy})_{i-\frac{1}{2},j+\frac{1}{2},k} \right] + \frac{1}{\delta y_{j+\frac{1}{2}}} [(\tau_{nyy})_{i,j+1,k} - (\tau_{nyy})_{i,j,k}] \\ &\quad + \frac{1}{\delta y_{j+\frac{1}{2}}} [(\tau_{nyy})_{i,j+1,k} - (\tau_{nyy})_{i,j,k}] + \frac{1}{\delta y_k} \left[(\tau_{nzy})_{i,j+\frac{1}{2},k+\frac{1}{2}} - (\tau_{nzy})_{i,j+\frac{1}{2},k-\frac{1}{2}} \right] \end{aligned} \quad (18b)$$

$$\begin{aligned} (\nabla \tau_{nz})_{i,j,k+\frac{1}{2}} &= \frac{1}{\delta x_i} \left[(\tau_{nxz})_{i+\frac{1}{2},j,k+\frac{1}{2}} - (\tau_{nxz})_{i-\frac{1}{2},j,k+\frac{1}{2}} \right] + \frac{1}{\delta y_j} \left[(\tau_{nyz})_{i,j+\frac{1}{2},k+\frac{1}{2}} - (\tau_{nyz})_{i,j-\frac{1}{2},k+\frac{1}{2}} \right] \\ &\quad + \frac{1}{\delta z_k} [(\tau_{nzz})_{i,j,k+1} - (\tau_{nzz})_{i,j,k-1}] \end{aligned} \quad (18c)$$

As explained earlier, the angular brackets represent the donor cell differenced quantities. In the momentum equations, the gas pressure and the drag terms are implicitly differenced. Also note that the drag terms are linearly implicit which is necessary for the particular method of solution adopted here.

Eqs. (12), (14), (16a), (16b) and (16c) form $4N + 1$ coupled nonlinear algebraic relations for the $4N + 1$ variables: P_g , ε_n , u_n , v_n , and w_n . The solids pressure, P_s , is related to its volume fraction by Eq. (10) and the phase volume fractions add up to 1.0. At each computational cycle, their values are updated by solving the finite difference equations.

A.2. The solution technique

An iterative technique is used to solve the finite difference equations given in Section A.1. To facilitate the particular method of solution the equations are recast in the following form. The momentum equations can be collected together in a matrix form. The formulation below is generalized into N phases. When $l = g, s$, it collapses to the two-phase gas–solids solution technique. Thus, Eq. (16a) gives:

$$\mathbf{AU} = \mathbf{C}_u \quad (19)$$

where

$$\mathbf{A} = \begin{bmatrix} \delta t \sum_{l=1}^N \beta_{1l} + \varepsilon_1 \rho_1 & -\delta t \beta_{12} & \cdots & -\delta t \beta_{1N} \\ -\delta t \beta_{21} & \delta t \sum_{l=1}^N \beta_{2l} + \varepsilon_2 \rho_2 & \cdots & -\delta t \beta_{2N} \\ \vdots & \vdots & \ddots & \vdots \\ -\delta t \beta_{N1} & -\delta t \beta_{N2} & \cdots & \delta t \sum_{l=1}^N \beta_{Nl} + \varepsilon_N \rho_N \end{bmatrix} \quad (19a)$$

$$\mathbf{U} = \begin{bmatrix} u_1 \\ u_2 \\ \vdots \\ u_N \end{bmatrix} \quad (19b)$$

$$\mathbf{C}_u = \begin{bmatrix} \left(\overline{\varepsilon_1 \rho_1 u_1} \right) - \frac{\delta t}{\delta x_{i+\frac{1}{2}}} \left((p_n)_{i+1,j,k} - (p_n)_{i,j,k} \right)^{n+1} \\ \left(\overline{\varepsilon_2 \rho_2 u_2} \right) - \frac{\delta t}{\delta x_{i+\frac{1}{2}}} \left((p_n)_{i+1,j,k} - (p_n)_{i,j,k} \right)^{n+1} \\ \vdots \\ \left(\overline{\varepsilon_N \rho_N u_N} \right) - \frac{\delta t}{\delta x_{i+\frac{1}{2}}} \left((p_n)_{i+1,j,k} - (p_n)_{i,j,k} \right)^{n+1} \end{bmatrix} \quad (19c)$$

Eq. (16b) gives

$$\mathbf{A}\mathbf{V} = \mathbf{C}_v \quad (20)$$

where

$$\mathbf{V} = \begin{bmatrix} v_1 \\ v_2 \\ \vdots \\ v_N \end{bmatrix} \quad (20a)$$

$$\mathbf{C}_v = \begin{bmatrix} \left(\overline{\varepsilon_1 \rho_1 v_1} \right) - \frac{\delta t}{\delta y_{j+\frac{1}{2}}} \left((p_n)_{i,j+1,k} - (p_n)_{i,j,k} \right)^{n+1} \\ \left(\overline{\varepsilon_2 \rho_2 v_2} \right) - \frac{\delta t}{\delta y_{j+\frac{1}{2}}} \left((p_n)_{i,j+1,k} - (p_n)_{i,j,k} \right)^{n+1} \\ \vdots \\ \left(\overline{\varepsilon_N \rho_N v_N} \right) - \frac{\delta t}{\delta y_{j+\frac{1}{2}}} \left((p_n)_{i,j+1,k} - (p_n)_{i,j,k} \right)^{n+1} \end{bmatrix} \quad (20b)$$

Eq. (16c) gives:

$$\mathbf{A}\mathbf{W} = \mathbf{C}_w \quad (21)$$

where

$$\mathbf{W} = \begin{bmatrix} w_1 \\ w_2 \\ \vdots \\ w_N \end{bmatrix} \quad (21a)$$

$$\mathbf{C}_w = \begin{bmatrix} (\overline{\varepsilon_1 \rho_1 w_1}) - \frac{\delta t}{\delta y_{k+\frac{1}{2}}} ((p_n)_{i,j,k+1} - (p_n)_{i,j,k})^{n+1} \\ (\overline{\varepsilon_2 \rho_2 w_2}) - \frac{\delta t}{\delta y_{k+\frac{1}{2}}} ((p_n)_{i,j,k+1} - (p_n)_{i,j,k})^{n+1} \\ \vdots \\ (\overline{\varepsilon_N \rho_N w_N}) - \frac{\delta t}{\delta y_{k+\frac{1}{2}}} ((p_n)_{i,j,k+1} - (p_n)_{i,j,k})^{n+1} \end{bmatrix} \quad (21b)$$

The gas continuity equation ((14) for $n = g$) can be written as

$$D_{i,j,k} = -(\varepsilon_g \rho_g)_{i,j,k}^{n+1} + (\varepsilon_g \rho_g)_{i,j,k}^n - \frac{\delta t}{\delta x_i} \langle (\varepsilon_g \rho_g) u_g \rangle_{i,j,k}^{n+1} - \frac{\delta t}{\delta y_j} \langle (\varepsilon_g \rho_g) v_g \rangle_{i,j,k}^{n+1} - \frac{\delta t}{\delta z_k} \langle (\varepsilon_g \rho_g) w_g \rangle_{i,j,k}^{n+1} \quad (22)$$

where $D_{i,j,k}$ is the residue of the gas continuity equation, which should be equal to 0 for absolute convergence. To solve the finite difference equations the pressure in each computational cell is corrected iteratively such that $D_{i,j,k}$ meets a convergence criterion. The iterations are continued till the convergence criterion is met in all the computational cells simultaneously.

The details of this iterative procedure are given below.

- (1) Calculate the tilde quantities using Eqs. (17a), (17b) and (17c).
- (2) Calculate the drag coefficients.
- (3) Calculate the new time level velocities using Eqs. (16a), (16b) and (16c).
- (4) Calculate $\alpha_{i,j}$, approximate given by

$$\begin{aligned} \frac{1}{\alpha_{i,j,k}} &= \frac{\partial D_{i,j,k}}{\partial (p_g)_{i,j,k}} = \frac{\varepsilon_g}{(C_g)_{i,j,k}^2} + \frac{(\delta t)^2}{(\delta x_i)^2} \left[(\varepsilon_g)_{i+\frac{1}{2},j,k} + (\varepsilon_g)_{i-\frac{1}{2},j,k} \right] + \frac{(\delta t)^2}{(\delta y_j)^2} \left[(\varepsilon_g)_{i,j+\frac{1}{2},k} + (\varepsilon_g)_{i,j-\frac{1}{2},k} \right] \\ &\quad + \frac{(\delta t)^2}{(\delta z_k)^2} \left[(\varepsilon_g)_{i,j,k+\frac{1}{2}} + (\varepsilon_g)_{i,j,k-\frac{1}{2}} \right] \end{aligned} \quad (23)$$

(5) Correct the pressure iteratively. Pressure corrections are done in a cell till convergence is obtained or the number of iterations exceed an inner iterations limit. Then the computations proceed till the entire computational regime is covered. At the end of such a computational sweep, if convergence was not obtained in any of the cells, the sweeps are repeated. The number of such sweeps are restricted by an outer iterations limit. The iterative procedure for a single cell involves the following steps.

(a) Calculate $D_{i,j,k}$ using Eq. (23). If $|D_{i,j,k}| < \delta_g$, go to step (e) where δ_g is a small positive value. Here, we let $\delta_g = 5 \times 10^{-4}$.

(b) If $|D_{i,j,k}| > \delta_g$, the pressure in the cell needs to be adjusted. Initial adjustments are done using Newton's method,

$$(p_g)_{i,j,k}^{m+1} = (p_g)_{i,j,k}^m - \omega \alpha_{i,j,k} D_{i,j,k} \quad (24)$$

where ω is a relaxation parameter near unity. Newton's method is continued till $D_{i,j,k}$ changes sign. After $D_{i,j,k}$ changes sign, the next pressure correction is done using a secant method. Thereafter the pressure corrections are done using a constrained two-sided secant method. These three methods are described in detail by Lyczkowski et al. [5].

(c) Calculate the velocities using Eqs. (16a), (16b) and (16c).

(d) Calculate the mass fluxes.

(e) Solve the solids continuity equation (14) for ε_n ($n = s$).

(f) Using Eq. (2), find the new value of ε_g .

(g) If $|D_{i,j,k}| > \delta_g$ go to step (a).

References

- [1] J.X. Bouillard, R.W. Lyczkowski, S.M. Folga, D. Gidaspow, G.F. Berry, *Can. J. Chem. Eng.* 67 (1989) 218.
- [2] J.X. Bouillard, R.W. Lyczkowski, D. Gidaspow, *AIChE J.* 35 (6) (1989) 908.
- [3] D. Gidaspow, *Multiphase Flow and Fluidization. Continuum and Kinetic Theory Descriptions*, Academic Press, San Diego, CA (1994).
- [4] I.K. Gamwo, Y. Soong, D. Gidaspow, R.W. Lyczkowski, in: K.J. Heinschel (Ed.), *Proc. 13th Int. Conf. on Fluidized Bed Combustion*, Vol. 1, American Society of Mechanical Engineers, New York (1995), pp. 297–303.
- [5] R.W. Lyczkowski, J.X. Bouillard, S.M. Folga, *Users' manual for FLUFIX/MOD2: a computer program for fluid–solids hydrodynamics*, Argonne National Laboratory Sponsor Report, Argonne, IL (April 1992). Reprinted by USDOE METC as DOE/MC/24193-3491/NTIS No. DE94000033, available from NTIS, Springfield, VA (1994).
- [6] J.W. Pritchett, T.R. Blake, S.K. Garg, *A numerical model of gas fluidized beds*, *AIChE Symp. Series* 74, No. 176, American Institute of Chemical Engineers, New York (1989), pp. 124–148.
- [7] A. Padhye, T.J. O'Brien, *Computer simulation of cold flow studies of the Westinghouse gasifier*, preprint, 7th Annual Energy Source Technology Conf. Exhibition (1984).
- [8] M. Syamlal, D. Gidaspow, *AIChE J.* 31 (1985) 127.
- [9] D. Gidaspow, B. Ettehadieh, *Ind. Eng. Chem. Fundam.* 22 (1983) 193.
- [10] D. Gidaspow, B. Ettehadieh, J.X. Bouillard, *Hydrodynamics of fluidization: bubbles and gas compositions in the U-gas process*, *AIChE Symposium Series* 80, No. 241, American Institute of Chemical Engineers, New York (1985), pp. 57–64.
- [11] D. Gidaspow, M. Syamlal, Y.C. Seo, *Hydrodynamics of Fluidization of single and binary size particles: supercomputer modeling*, in: K. Ostergaard, A.S. Sorensen (Eds.), *Fluidization V: Proceedings of the 5th Engineering Foundation Conference on Fluidization*, Engineering Foundation (1986), pp. 1–8.
- [12] D. Gidaspow, Y.T. Shi, J.X. Bouillard, D. Wasan, *AIChE J.* 35 (1989) 714.
- [13] F. Concha, M.C. Bustos, *AIChE J.* 33 (1987) 312.
- [14] O. Molerus, *Powder Technol.* 12 (1975) 259.
- [15] K. Rietema, S.M.P. Mutsers, *Proc. Int. Symp. on Fluidization*, Toulouse, France (1973), pp. 32–33.
- [16] H.W. Piepers, E.J.E. Cottar, A.H.M. Verkooijen, K. Rietema, *Powder Technol.* 37 (1984) 55.
- [17] K. Shinohara, *Rheological property of particulate solids*, in: M.E. Fayed, L. Otten (Eds.), *Handbook of Powder Science and Technology*, Van Nostrand-Reinhold, New York (1984), pp. 129–169.
- [18] C. Orr Jr., *Particulate Technology*, Macmillan, New York (1966), p. 421.
- [19] Y.H. Ai, *Solids velocity and pressure fluctuation measurements in air-fluidized beds*, MS Thesis, University of Illinois at Urbana, Champaign, IL (1990).
- [20] I.K. Gamwo, *Multi-dimensional hydrodynamic and erosion modeling of fluidized beds*, PhD Dissertation, Illinois Institute of Technology, Chicago, IL (1992).
- [21] R.W. Lyczkowski, I.K. Gamwo, F. Dobran, Y.H. Ai, B.T. Chao, M.M. Chen, D. Gidaspow, *Powder Technol.* 76 (1993) 65.
- [22] I.K. Gamwo, Y. Soong, R.R. Schehl, M.F. Zarochak, R.W. Lyczkowski, *Proc. NOBCCChE '94*, Vol. 21 (1994) 183–190.
- [23] K. Rietema, *The Dynamics of Fine Powders*, Elsevier Applied Science, London (1991), pp. 166–173.
- [24] B. Singh, T.G. Callcott, G.R. Rigby, *Powder Technol.* 20 (1978) 99.
- [25] F.H. Harlow, A.A. Amsden, *J. Comp. Phys.* 17 (1975) 19.
- [26] W.C. Rivard, M.D. Torrey, *K-FIX: a computer program for transient, two-dimensional, two-fluid flow*, Los Alamos National Laboratory Report, LA-NUREG-6623, Los Alamos (1977).
- [27] W.C. Rivard, M.D. Torrey, *K-FIX: a computer program for transient, two-dimensional, two-fluid flow-THREED: an extension of the K-FIX code for three-dimensional calculations*, Los Alamos National Laboratory Report, LA-NUREG-6623, Suppl. II, Los Alamos (1979).
- [28] M. Syamlal, *Multiphase hydrodynamics of gas–solids flow*, PhD Dissertation, Illinois Institute of Technology, Chicago, IL (1985).
- [29] M. Syamlal, W. Rogers, T.J. O'Brien, *MFIX Documentation: Theory Guide*, Technical Note, DOE/METC-94/1004, NTIS/DE94000087, National Technical Information Service, Springfield, VA (1993).
- [30] H. Enwald, E. Pierano, A.-E. Almstedt, *Int. J. Multiphase Flow* 22 (1966) 21, Suppl.